Soot Formation in Methane Pyrolysis Reactor: Modeling Soot Growth and Particle Characterization

Akash Bhimrao Shirsath, Manas Mokashi, Patrick Lott, Heinz Müller, Reihaneh Pashminehazar, Thomas Sheppard, Steffen Tischer, Lubow Maier, Jan-Dierk Grunwaldt, and Olaf Deutschmann*

ABSTRACT: Methane pyrolysis is a very attractive and climate-friendly process for hydrogen production and the sequestration of carbon as solid material. The formation of soot particles in methane pyrolysis reactors needs to be understood for technology scale-up calling for appropriate soot growth models. A monodisperse model is coupled with a plug flow r eactor m odel and elementary-step reaction mechanisms to numerically simulate processes in methane pyrolysis reactors, namely, the chemical conversion of methane to hydrogen, formation of C−C coupling products and polycyclic aromatic hydrocarbons, and growth of soot particles. The soot growth model accounts for the effective structure of the aggregates by calculating the coagulation frequency from the free-molecular regime to the continuum regime. It predicts the soot mass, particle number, area, and volume concentration, along with the particle size distribution. For comparison, experiments on methane pyrolysis are carried out at different temperatures and collected soot samples are characterized using Raman spectroscopy, transmission electron microscopy (TEM), and dynamic light scattering (DLS).

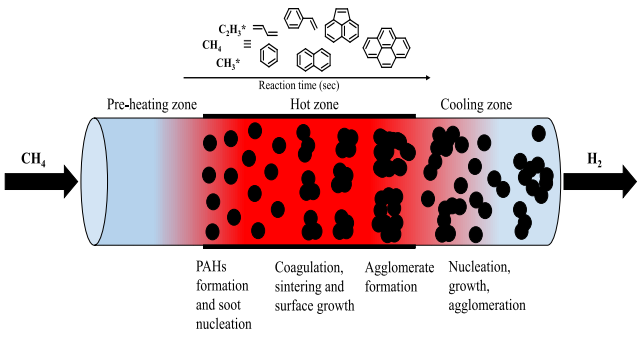

INTRODUCTION

Natural gas as the least polluting fossil fuel has a wide variety of applications such as heating and power generation by direct combustion, chemical feed-stock, and the production of syngas, usually via steam re-forming and recently also more climate-friendly via dry re-forming using CO_2 as reactant.[1−3] Pyrolysis of natural gas is another alternative method of making hydrogen; 96% of it is methane. Biomass-derived methane could even result in negative greenhouse gas emissions with the pyrolysis process since the thermal decomposition of methane under oxygen-free conditions breaks CH_4 directly into hydrogen and solid carbon. As solid carbon is the only byproduct of the pyrolysis process, no further treatments, storage, or CO_2 separation are needed for a climate-friendly process chain.[4−6] As a result of pyrolysis, solid carbon can take various forms, such as graphite-like layers on walls, infiltrated into carrier materials, and soot particles.[7−12] Soot formation occurs due to the formation of polycyclic aromatic hydrocarbons (PAHs).[13−16] Previous studies have found that the particle number concentration of soot formed during pyrolysis is directly related to processing conditions, hydrocarbon concentration and exponentially related to temperature.[17,18] While tremendous progress has been made in understanding the physical and chemical processes responsible for soot formation, some questions remain.[19]

Nucleation of soot particles occurs as a result of a complex series of chemical reactions, followed by coagulation, sintering, surface growth, and condensation.[20] A detailed gas-phase kinetics model, fluid dynamics, and transport processes can be combined with the model of soot formation to gain better insights. However, computing speed may be compromised. Due to this, many approaches to approximate the general equations of dynamics have been proposed. Among them are the monodisperse model,[21−24] the moment method,[19,25−27] the sectional method,[28−30] the stochastic model,[27,31] and the Galerkin model.[32]

The formation of soot is now widely accepted to be caused by PAHs, contrary to earlier scientific discussions. The equilibrium model cannot predict soot formation since it is

kinetically controlled. Frenklach et al.[13,20,25] developed detailed chemical kinetics for nucleation and growth of soot particles via PAHs. The method of moment was applied to the study of the formation and growth of soot agglomerates.[25] Furthermore, a number of experimental and numerical studies indicate the role of PAHs in soot nucleation.[33−35] A soot model based on the method of moment was developed by Wang et al.[36] for the formation of soot in the counter-flow diffusion flame of ethylene and its binary mixture using the PAHs growth mechanism, which was mainly proposed for gaseous fuels with C_1-C_4.[37] At high temperatures, physical dimerization cannot be a crucial step in soot formation because of the equilibrium of reaction with PAHs. Sabbah et al.[38] explore the role of PAHs in soot formation. The two-three-ring thermodynamic barrier is crossed by pyrene, which leads us to conclude that particle inception begins with pyrene.[14,39] Moreover, pyrene dimers were further investigated for their role in nucleating soot.[18,25,34,40−42] Kraft et al.[43,44] developed several detailed soot models which include coagulation, sintering, inception, surface growth, and other factors. Among other factors that may contribute to soot formation, Tsantilis et al.[45] and Zacharias et al.[46] also covered sintering. Chen et al.[47] include sintering in a detailed soot population balance model to simulate the premixed flame. Sander et al.[48] then applied the model to polydispersed nanoparticle agglomerations. In addition, experiments confirm that coagulation plays a crucial role in soot formation.[25,35,49,50] For predicting the size and structure of soot particles, Park et al.[30,51] developed a series of subroutines based on moving and fixed sectional methods. However, particle sintering was not taken into account in the studies. Although Morgan et al.[52] claimed that sintering, which is critical for inorganic materials, is unlikely to be relevant in the context of soot formation, recent studies provide experimental[53] and theoretical[43,47,54] evidence for the sintering of soot particles.

A monodisperse model can calculate average particle properties based on total concentrations, mass, and area.[21] Assuming spherical particles, Leung et al.[55] proposed a monodisperse 2-equation model system. Kruis et al.[24] extended a 3-equation monodisperse model to account for the fractal structure of soot aggregates during coagulation and sintering. Alternatively, Tsantilis and Pratsinis further elaborated on monodisperse models by adding chemical kinetics, coagulation, sintering, surface growth, and fractal dimension.[21,56] Kholghy et al.[57] investigated the formation of carbon black using a monodisperse population balance model that included surface growth, coagulation, and oxidation. An in-depth discrete element model is used to explain the fractal-like morphology of soot aggregates.

To investigate soot formation, the monodisperse population balance model is coupled with a one-dimensional plug flow reactor model within the DETCHEM software package.[58] Based on Appel, Bockhorn, and Frenklach's (ABF) chemical kinetics, the present model simulates methane pyrolysis in the plug flow reactor.[13] In the proposed model, simultaneous chemical reactions, coagulation, and sintering are taken into account. Additionally, collision frequency, primary particle diameter, and average number of primary particles per aggregate are examined in terms of fractal-like dimensions. Results from experimental measurements and characterization are compared with those predicted from the simulation.

EXPERIMENTAL METHODOLOGY

Experiments. Experiments were conducted in a high-temperature−pressure reactor that was designed for kinetic measurements at temperatures of up to 2073 K and at pressures of up to 10 bar as previously described in detail by Angeli et al.[59] The reaction gas mixture was fed via mass flow controllers (Bronkhorst) and was preheated at around 443 K in stainless-steel tubes. The α-Al_2O_3 tubular plug-flow reactor (diameter, 0.2 m; length, 1.0 m; Friatec, Aliaxis Deutschland GmbH) was placed in a stainless-steel vessel (Berg-idl GmbH) equipped with heating elements and insulation, which results in a hot zone of approximately 0.4 m. All setup parameters were controlled by an in-house developed LabView software. The effluent gas flow was monitored with an HPR-20 mass spectrometer (Hiden Analytical). For the present study, under atmospheric pressure, an inlet reaction gas mixture containing H_2 and CH_4 in a molar ratio of 2:1 and a gas flow resulting in a residence time of 5 s in the hot zone was chosen, while continuously analyzing the H_2, CH_4, C_2H_2, C_2H_4, C_2H_6, and C_6H_6 content in the outlet gas stream. Finally, soot was collected with a filter at the reactor bottom, shown in Figure 1.

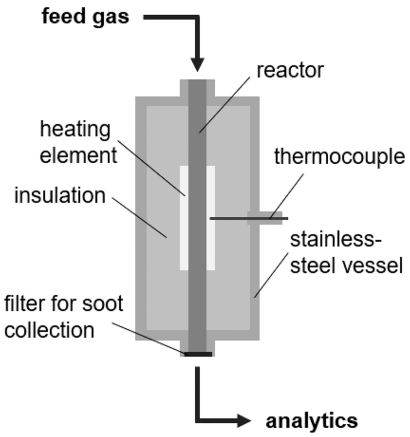

Figure 1. Experimental setup for methane pyrolysis, which can be operated at temperatures of up to 2073 K and pressures of up to 10 bar.

Characterization. The collected soot samples at the end of the reactor at different time intervals, 1, 5, 10, and 20 min, were analyzed using various characterization methods. Diffraction techniques are usually the methods of choice for the structural characterization of highly ordered solid materials (crystalline long-range order). For highly disordered materials such as soot, Raman spectroscopy is well suited because it is sensitive not only to crystal structures but also to molecular structures (short-range order). Therefore, the Raman spectrum allows for predicting the different carbon allotropes and disordered varieties.[60−62] Microscopic Raman spectroscopy was performed using a Renishaw inVia Reflex Spectrometer System equipped with a He-Ne laser at 633 nm (about 25 mW at the source) and a research-grade Leica microscope. For all samples, a 50× objective and a grating with 600 lines mm^{-1} were used resulting in a spectral range of approximately 400−3600 cm^{-1}. An area of 65 μm × 65 μm was raster scanned with a step size of 1.3 μm resulting in 2500 individual spectra. Raman spectroscopy data were recorded with the laser shape adjusted to a line at the sample position and the laser intensity set to 10%. Data treatment was performed with WiRE 4.4 from

Renishaw. Finally, all individual spectra were averaged to a single spectrum.

In order to gain information about the soot aggregate and primary particle sizes, transmission electron microscopy (TEM) and dynamic light scattering (DLS) analysis were conducted. TEM analysis provides an overview of the aggregate shape and the size of primary particles. TEM images were acquired using a Philips Tecnai F20 microscope. Small amounts of soot diluted in ethanol were transferred onto TEM grids for scanning. DLS analysis was performed by a Zetasizer Nano Series device (Malvern Instruments Ltd.), which measures the Brownian motion and relates this to the size of the particles, i.e., the hydrodynamic diameter. For this, the particles were illuminated with laser radiation and the intensity fluctuations in the scattered light were analyzed. Soot particles were dissolved in water and homogenized with an ultrasonic disperser to ensure a homogeneous sample solution without any sedimentation.

MODEL

Gas-Phase Chemistry. An elementary step-based gas-phase reaction mechanism is used to simulate methane pyrolysis (Appel et al., ABF).[13] Under oxidation and pyrolysis conditions, the reaction mechanism was proposed primarily for C_1 and C_2 hydrocarbons. Through carbon−carbon coupling reactions, benzene and linear hydrocarbons are formed. In addition, the chemical kinetics includes reactions with polycyclic aromatic hydrocarbons (PAHs) (up to pyrene ($C_{16}H_{10}$)). It consists of 544 reactions and 101 species in the gas phase. Dimers are then assumed to form when the PAH species collide. As a result of these dimers, soot clusters are formed. Based on the assumption that pyrene is primarily responsible for the overcoming of the two-three ring thermodynamic barrier, the dimer is therefore assumed to be responsible for soot nucleation.[14,40] In addition, the reaction shown in eq 1 was implemented into the present reaction scheme using the data published by Kholghy et al.[63] For the monodisperse soot model, the chemical source term is provided by the net production rate of the dimer.

$$C_{16}H_{10} + C_{16}H_{10} \rightarrow \text{Dimer} \tag{1}$$

The forward reaction rate, k (m^3/s), constant for the above is given by

$$k = E_d \times {d_d}^2 \times \sqrt{8\pi k_B T / M_d} \tag{2}$$

where E_d is the enhancement factor of 2.2, d_d is an effective diameter of dimer, and M_d is the reduced mass of the dimer.

Plug Flow Reactor. Methane pyrolysis experiments were simulated using a 1D plug flow reactor model. A plug flow reactor model in the form of FORTRAN code is coupled with the DETCHEM software package.[58,64,65] A 1D plug flow reactor model simulates the chemically reacting flow of a gas mixture at steady-state conditions. Assuming no change in radial properties, axial changes in gas properties are allowed. It solves continuity equations, species conservation equations, energy equations, and equations of state. This system of differential equations was solved with the differential-algebraic solver, LIMEX.[66]

Equation 3 of continuity is defined as

$$\frac{\mathrm{d}(\rho u)}{\mathrm{d}z} = P' \sum_{i \in S_g} M_i \dot{s}_i \tag{3}$$

where ρ is the gas-phase density (kg/m^3), z is the axial coordinate of the reactor (m), A_c is the cross-sectional area (m^2), u is the flow velocity (m/s), $\dot{s}_i$ is the surface reaction rate at the reactor wall for species i ($mol/m^2/s$), P' is the chemically active perimeter per unit length (1/m), and M_i is the molar mass of species i (kg/mol). Furthermore, under steady-state conditions, the above eq 3 is equal to zero, i.e., no mass flux from or to the reactor wall.

Equation 4 stands for the species conservation equation:

$$\rho u \frac{\mathrm{d}Y_i}{\mathrm{d}z} + Y_i P' \sum_{i \in S_g} M_i \dot{s}_i = M_i (P' \dot{s}_i + \dot{\omega}_i) \tag{4}$$

where Y_i is the mass fraction of species i and $\dot{\omega}_i$ is the gas-phase reaction rate for species i ($mol/m^3/s$).

Equation 5 is used for the energy balance:

$$\rho u A_c \frac{C_p \mathrm{d}(T_g)}{\mathrm{d}z} + A_c \sum_{i \in S_g} M_i \dot{\omega}_i h_i + P \sum_{i \in S_g} M_i \dot{s}_i h_i = PU(T_w - T_g) \tag{5}$$

where C_p is the heat capacity (J/kg/K), T_w is the reactor wall temperature (K), h_i is the specific enthalpy of species i (J/kg), T_g is the gas temperature (K), U is the overall heat transfer coefficient ($W/m^2/K$), and P is the perimeter of duct (m).

However, for the present study, terms related to the $\dot{s}_i$ terms can be neglected as no surface reactions are considered. Furthermore, eq 5 can be replaced by the experimentally measured temperature profile in the reactor. Therefore, no energy balance is solved.

Monodisperse Model. For the investigation of soot particle growth, the monodisperse model takes different processes into account, simultaneous chemical reaction, coagulation, and sintering. Also, the model has coupled with the plug flow reactor model described above. The equation system of the monodisperse model consists of total particle number concentration (N, $1/{m_{gas}}^3$), particle surface area concentration (A, $m^2/{m_{gas}}^3$) and particle volume concentration (V, $m^3/{m_{gas}}^3$). Also, the equation system is used for further calculations of primary particle diameter (d_p, m), collision diameter (d_c, m), gyration diameter (d_g, m), and mobility diameter (d_m, m).

The rate of change of particle concentration N is increased due to the formation of particles via chemical reaction and reduced due to coagulation:

$$\frac{\mathrm{d}N}{\mathrm{d}t} = -\frac{\mathrm{d}C_{soot}}{\mathrm{d}t} N_A - \frac{1}{2}\beta N^2 \tag{6}$$

where $-\mathrm{d}C_{soot}/\mathrm{d}t$ is the rate of formation of pyrene dimers ($mol/m^3/s$), N_A is the Avogadro number, and β is the Brownian coagulation coefficient (m^3/s). For the present study, the coagulation coefficient is calculated based on the Fuchs interpolation method from the free-molecular regimes to continuum regimes.[24,67] The coagulation constant further accounts for the effect of an agglomerate structure by involving the collision diameter of the particle. The coagulation coefficient is calculated as

$$\beta = 4\pi d_c D \left[\frac{\frac{1}{2} d_c}{d_c + \sqrt{2}g} + \frac{\sqrt{2}D}{c\frac{1}{2} d_c} \right]^{-1} \tag{7}$$

$$c = \sqrt{\frac{8k_BT}{\pi m}} \tag{8}$$

$$Kn = \frac{2\lambda}{d_c} \tag{9}$$

$$g = \frac{[(d_c + L)^3 - (d_c^2 + L^2)^{3/2}]}{3Ld_c} - d_c \tag{10}$$

where D is the particle diffusion coefficient (m^2/s), k_B is the Boltzmann constant, g is the transition parameter, Kn is the Knudsen number, λ is the mean free path, L is the length scale, and c is the particle velocity (m/s). Furthermore, the rate of change of the particle surface area concentration eq 11 and particle volume concentrations eq 12 are, respectively

$$\frac{dA}{dt} = -\frac{dC_{soot}}{dt}N_A\alpha_m - \frac{1}{\tau_s}(A - N\alpha_s) \tag{11}$$

$$\frac{dV}{dt} = -\frac{dC_{soot}}{dt}N_A v_m \tag{12}$$

where α_s is the surface area of completely fused particle of volume V/N and v_m and α_m are the volume (m^3) and surface area (m^2) of soot monomer (pyrene dimer). Also, the general characteristics sintering time τ_s (s) is given in the form of Arrhenius's equation:[43,45]

$$\tau_s = 1.1 \times 10^{-14} d_p \exp\left(\frac{9.61 \times 10^4}{T}\left(1 - \frac{1.58 \times 10^{-9}}{d_p}\right)\right) \tag{13}$$

In the present model, the collision diameter of agglomerates is

$$d_c = \left(\frac{6V}{A}\right)\left(\frac{A^3}{36\pi NV^2}\right)^{1/D_f} = d_p(n_p)^{1/D_f} \tag{14}$$

where D_f is the mass fractal dimension and n_p is the number of primary particles per agglomerate. Assuming that particles are formed by cluster−cluster agglomeration, a value of 1.8 for D_f is used for the current study.[68] The following equations are used for the calculation of agglomerates mobility diameter (d_m) and gyration diameter (d_g):[69]

$$\frac{d_m}{d_p} = n_p^{0.45} \tag{15}$$

$$\frac{d_m}{d_g} = \begin{cases} \frac{1}{n_p^{0.2}} + 0.4, \text{ if } n_p > 1.8 \\ \sqrt{5/3}, \text{ if } n_p \leq 1.8 \end{cases} \tag{16}$$

The conditions for present reactor simulations are obtained from the experiments and discussed in the next section. Furthermore, for monodisperse model initial particle concentration (N_0) of 1×10^{16}, primary particle diameter (d_p) of 2 nm, soot particle density (ρ_{soot}) of 1800 kg/m^3, and fractal dimension (D_f) of 1.8. The net production rate of a pyrene dimer, computed via the plug flow reactor model, provides a chemical source term for the present monodisperse model.

RESULTS AND DISCUSSION

Gas-Phase Species Predictions. For testing the model approach, experiments were conducted at atmospheric pressure, 2:1 molar ratio of H_2:CH_4, 17.5 s total residence time, and 5 s in the hot zone. The reactor is 1 m long, with a 0.4 m hot zone after a 0.35 m preheating zone. During the experiments, three hot zone temperature conditions are used: 1473, 1673, and 1873 K. Simulations are based on temperature profiles determined experimentally, shown in Figure 2.

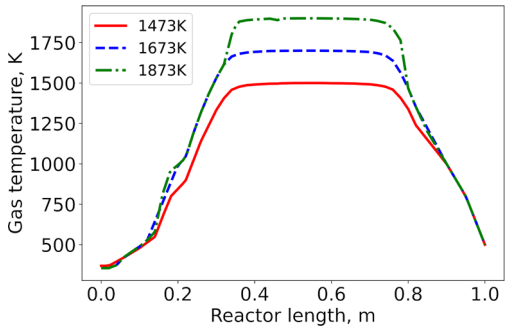

Figure 2. Experimentally measured temperature profiles. Solid line: 1473 K. Dashed line: 1673 K. Dashed-dotted line: 1873 K.

Table 1 shows the comparison between experimental and numerical results with their respective standard deviations (all values are rounded to 3 decimal places). The standard deviation between experimental and numerical values was calculated as the square root of the average of the squared differences of the points from the mean. In addition, the simulation results presented in this section are based solely on gas-phase results and are not connected to the soot model.

The comparison between numerically predicted and experimentally measured major gas-phase species, H_2 and CH_4, shows good agreement, as shown in Table 1. The majority of the methane is converted into hydrogen and C−C coupling products including soot and solid carbon materials. A methane conversion of approximately 90% has been observed in experiments with the temperature profiles depicted in Figure 2. An interesting feature is also revealed by the present experimental and simulation results at 1673 K. At 1673 K, methane conversion is highest due to thermodynamic restrictions. At 1873 K, the conversion of methane decreases.

The numerically predicted results, however, differ from experimentally measured minor species, C_2H_4, C_2H_6, and C_6H_6, as illustrated in Table 1. The numerically predicted minor species agree well with experimental findings at 1473 and 1673 K. In contrast, the deviation at 1873 K is larger. Furthermore, the simulation results show production of C_2H_2 around 0.2−0.4% for present conditions; however, experimentally measured C_2H_2 is around 0.001%. In general, soot surface growth is caused by C_2H_2 species.[70] However, during methane pyrolysis experiments using the same reactor that was used for the present study, besides soot formation, also graphitic sheet-like carbon formation occurred on the reactor walls;[71] in addition, the study uncovered the contribution of C_2H_2 species to deposited carbon based on a kinetic flow analysis. Furthermore, a majority of carbon was observed to be deposited on the reactor walls as graphite-like sheets, whereas only a small amount of soot was observed at the reactor outlet. Due to the fact that C_2H_2 species are almost completely

Table 1. Comparison of Experimental (exp) and Simulation (sim) Data for the Molar Fraction of End-of-Pipe Gas-Phase Species at 1473, 1673, and 1873 K with Standard Deviation (stdev)

T (K)	H_2_exp	H_2_sim	H_2_stdev	CH_4_exp	CH_4_sim	CH_4_stdev
1473	0.862	0.815	0.033	0.111	0.146	0.024
1673	0.945	0.886	0.041	0.035	0.078	0.030
1873	0.906	0.810	0.068	0.068	0.121	0.038
T (K)	C_2H_2_exp	C_2H_2_sim	C_2H_2_stdev	C_2H_4_exp	C_2H_4_sim	C_2H_4_stdev
1473	0.000	0.002	0.001	0.005	0.013	0.006
1673	0.000	0.002	0.001	0.003	0.011	0.006
1873	0.000	0.004	0.003	0.003	0.031	0.020
T (K)	C_2H_6_exp	C_2H_6_sim	C_2H_6_stdev	C_6H_6_exp	C_6H_6_sim	C_6H_6_stdev
1473	0.001	0.011	0.007	0.004	0.008	0.003
1673	0.001	0.010	0.007	0.000	0.004	0.002
1873	0.001	0.027	0.019	0.001	0.004	0.002

consumed in experiments, both the growth of soot surfaces and carbon deposition can be attributed to these species.

At hot zone temperatures of 1473, 1673, and 1873 K, the mole fraction of PAHs is numerically predicted along the reactor length with a total residence time of 17.5 s in the whole reactor (5 s residence time in the hot zone), as shown in Figure 3. Condensation of PAHs on soot particles occurs as a

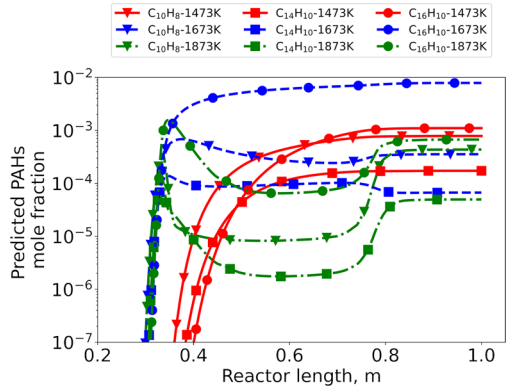

Figure 3. Numerically predicted axially resolved PAHs mole fraction at measured temperature profiles, 1473, 1673, and 1873 K. $C_{10}H_8$: ▼. $C_{14}H_{10}$: ■. $C_{16}H_{10}$: ●.

result of this formation of PAHs. There is a predominant PAHs formation in the hot zone of the reactor at the entrance region (after the first 0.35 m of reactor length). At lower temperatures, PAHs formation takes place slightly later in the reactor. As a result of cooling in the post hot zone (after 0.75 m of reactor length), reverse gas-phase reactions are occurring. Additionally, lowering the temperature in the post hot zone decreases the condensation of PAHs on soot particles. Therefore, as a result of the cooling, the PAHs concentration increases in the post hot zone of the reactor. Furthermore, the highest amount of PAHs is observed at a hot zone temperature of 1673 K compared to 1473 and 1573 K. This is primarily due to the thermodynamic limitations (Figure 3). As the simulations are conducted with a detailed kinetic model that includes reactions up to pyrene, the highest concentration of pyrene was achieved among other PAHs. For the nucleation of soot particles, the pyrene dimer was selected due to its high concentration and, as discussed previously, for its capability of forming large islands of stability.

In general, the numerically predicted mole fractions of major species agree well with our experimental measurements. As the soot model is not coupled with gas-phase chemistry, the predicted mole fractions of minor species show deviation.

Soot Formation. The formation of a dimer is a crucial step in the chemical mechanism that leads to soot inception. This assumption is often made for simplicity, as it allows the use of a single chemical source term in the soot model. The present soot model assumes a constant van der Waals enhancement factor (vdW) of 2.2 for the formation of pyrene dimers. However, the collision efficiency for dimer formation of small PAHs is typically quite small compared to the number of incipient soot particles that are formed during combustion. Small PAHs are small molecules and have low chances of a collision, as well as a low probability of colliding in the right orientation for bonding. Incipient soot particles, being much larger than PAHs, have a higher chance of collision, as well as a larger surface area, increasing the chances of bonding. Moreover, soot formation can help PAHs to overcome the limitations of their low collision efficiency. This is because they tend to stick to the surface of the soot, where they are more likely to collide with other PAHs, resulting in dimer formation. Using molecular dynamics simulations, Schuetz and Frenklach[40] studied the dimerization of pyrene via the collision of two pyrene molecules. They found that, at a temperature of 1600 K, approximately 15% of the collisions resulted in stable dimers and that the lifetime of these dimers exceeded 10 ps. This suggests that pyrene dimers may be able to serve as soot nuclei, at least under certain conditions. Furthermore, Hou et al.[43] used collision efficiencies to fit their experimental data on the size distribution of soot particles. They found that, at certain distances from the burner, a low collision efficiency of 0.2 was needed to fit the data for small nascent soot particles (diameter less than 8 nm), whereas a higher collision efficiency of 0.8 was needed to fit the data for large particles (diameter greater than 20 nm). However, they noted that these collision efficiencies were average values for all particles at a given distance from the burner and that small and large particles may have different collision efficiencies. In addition, it is also important to note that there are many other factors that can influence the formation of soot particles.

Soot nucleation rates are calculated using eq 1 for four different hot zone temperatures, 1473, 1573, 1673, and 1873 K, as shown in Figure 4. It is observed that the nucleation rate is lowest at 1473 K. The peak of the nucleation rate shifts toward the beginning of the hot zone as the temperature rises. Due to the lower amount of pyrene formed at 1873 K, the net production rate of pyrene dimer is smaller than that at lower temperatures (1473 and 1673 K) (Figure 3). To better

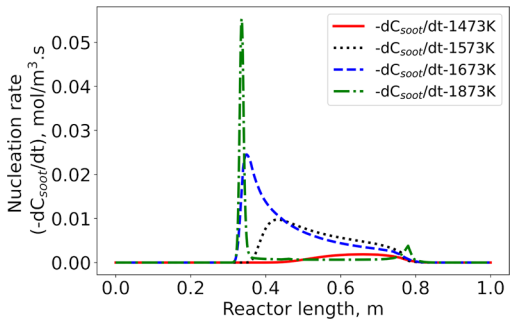

Figure 4. Nucleation rate of soot formation along reactor length. Solid line: 1473 K. Dotted line: 1573 K. Dashed line: 1673 K. Dashed-dotted line: 1873 K.

understand soot formation, an additional hot zone temperature of 1573 K was studied. Moreover, downstream of the hot zone, a small peak can be observed in nucleation rate at 1873 K, which can be explained by the sharp increase in the concentration of pyrene at 1873 K (Figure 3). At 1473 K, the nucleation rate is low, although a significant conversion of CH_4 is observed in both simulations and experiments.

The rate of change of the particle number concentration increases when soot is formed due to a chemical reaction, nucleation (Figure 5). As the nucleation rate equals the

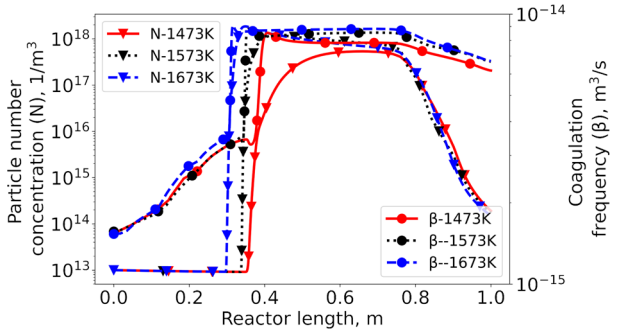

Figure 5. Particle number concentration (▼) and coagulation frequency (●) for soot formation along the reactor length. Solid line: 1473 K. Dotted line: 1573 K. Dashed line: 1673 K.

coagulation rate, the particle number concentration reaches its maximum. In addition, once the peak value is reached, the coagulation rate begins to dominate the soot formation process as the nucleation rate reduces along the hot zone and reaches low values after the hot zone. Thus, the total particle concentration is decreased and larger aggregates of soot particles are formed. Moreover, with increasing hot zone temperature, the particle number concentration peak shifts to the reactor's hot zone entrance. This is primarily caused by chemical reactions, i.e., the net production of pyrene dimers.

The growth of soot primary particle diameter (primary *y*-axis) as well as the growth of the soot mass (secondary *y*-axis) along the reactor length at different temperature profiles, 1473, 1573, and 1673 K, is shown in Figure 6. For all the temperature profiles, the largest primary particle diameter (of 19 nm) was observed at 1673 K, and the smallest (of 11 nm) at 1473 K. In addition, downstream of the hot zone, the soot primary particle diameter exhibits a constant pattern. The constant particle diameter suggests a complete dominance of coagulation and the formation of large agglomerates. Additionally, the unreacted C_2H_2 in the gas phase may contribute to

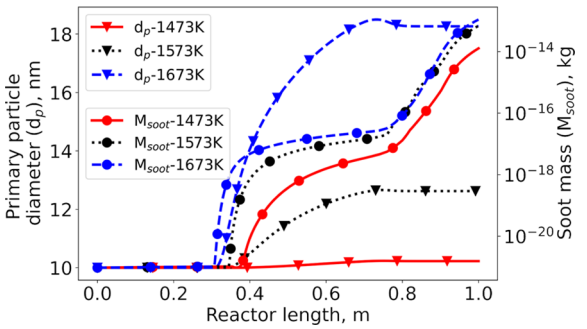

Figure 6. Primary particle diameter (▼) and soot mass (●) along the reactor length at different hot zone temperatures. Solid line: 1473 K. Dotted line: 1573 K. Dashed line: 1673 K.

the formation of agglomerates through the surface growth mechanism. Despite this, the present approach does not take soot surface growth into account. Thus, it is possible to assume that the present model underestimates the diameter of the primary particle.

The prediction of soot mass growth shows that soot mass increases initially due to the formation of new soot particles at the entrance of the hot zone, after the first 0.35 m, illustrated in Figure 6 (secondary *y*-axis). The growth in soot mass increased at a faster rate as the particles entered downstream of the hot zone due to the coagulation of particles. Additionally, the significant concentration of PAHs in the downstream hot zone suggests possible condensation/adsorption of PAHs on soot particles (Figure 3). It increases the soot mass further. Furthermore, the highest soot mass growth rate was observed at 1673 K. It can also be observed that soot mass growth accelerates as the temperature increases in the hot zone. It is explained by the net production rate of pyrene dimers, which form the primary soot particles. A slightly higher nucleation rate was observed at the hot zone temperature of 1573 K than at 1673 K at the beginning of the downstream hot zone (Figure 4). A comparison of the coagulation rate at 1573 and 1673 K shows only slight differences (Figure 5). There is an identical soot mass growth profile at the beginning of the hot zone downstream as a result of both of these phenomena. Due to the higher PAHs concentrations at 1673 K, the soot mass increases at a slightly faster rate than at 1573 K later on.

According to Figure 7, primary particles per aggregate increase very slowly downstream of the hot zone and rapidly near the reactor end. As seen in Figures 5 and 2, the sharp increase in primary particles per aggregate is mainly due to the

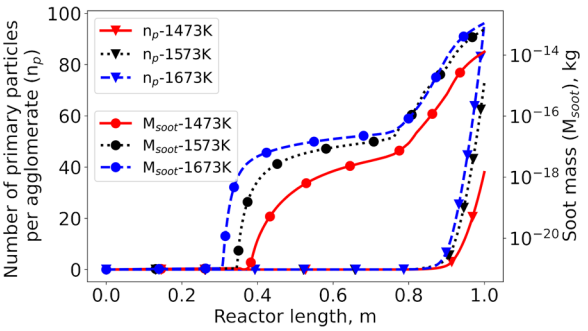

Figure 7. Number of primaries per aggregate (▼) and soot mass (●) along the reactor length at different temperatures. Solid line: 1473 K. Dotted line: 1573 K. Dashed line: 1673 K.

coagulation process and PAHs condensation. As a result of the surface growth mechanism, the number of primaries per aggregate increases. The present simulation does not take surface growth into account, so the number of primaries per aggregate is assumed to be underestimated.

As shown in Figure 8, the particle size distribution (PSD) of soot particles is based on mobility diameter, with a prediction

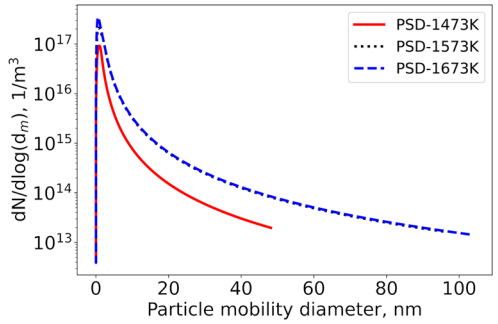

Figure 8. Predicted particle size distribution at end of reactor based on mobility diameter at different temperatures. Solid line: 1473 K. Dotted line: 1573 K. Dashed line: 1673 K.

at the end of the reactor. PSD predictions can reveal the processes involved in soot formation, especially for smaller particle sizes, since it is difficult to measure them experimentally. According to the PSD, the coagulation process dominates the reactor end, which results in a large number of particles being spared. The PSD shows a monomodal distribution due to the limitations of the current model (no soot surface growth).

As mentioned previously, the residence time is long enough for soot particles to coagulate and form aggregates, so coagulation becomes the dominant process rather than inception. As soot particles are in aggregate structures when sampled at the reactor outlet, the sintering process needs to be considered. The sintering rate is given by eq 13. To explore the impact of the sintering rate, the value of 1.58 nm for the critical particle diameter (d_{crit}) is varied while the values obtained from Chen et al.[47] for A_s and E_s are kept constant. The collision particle diameter is critical in determining the sintering process, above which the sintering equation is applied whereas lower values lead to instant coalescence of neighboring primary particles.[45] The sensitivity analysis showed that a decreasing in particle number concentration is accompanied by an increasing average primary particle diameter. A d_{crit} of 1.58, 5, and 10 nm yields primary particle diameters of 19, 40, and 65 nm, respectively, as shown in Figure 9. Additionally, the present analysis confirms findings by Hou et al.[43] who reported that the primary particle diameter has a high sensitivity with respect to the sintering rate.

Overall, the simplified monodisperse model effectively captures trends in the changes in nucleation rate, primary particle diameter, and soot mass growth with varying hot zone temperatures and provides valuable insight into the underlying mechanisms of soot formation. Furthermore, it is computationally less demanding, as tracking a large number of different-sized particles can become computationally infeasible as the number of particles increases. Nevertheless, due to the assumptions and limitations of the monodisperse model, it is critical to compare the results of the model with other more complex models to check the validity of the assumptions made.

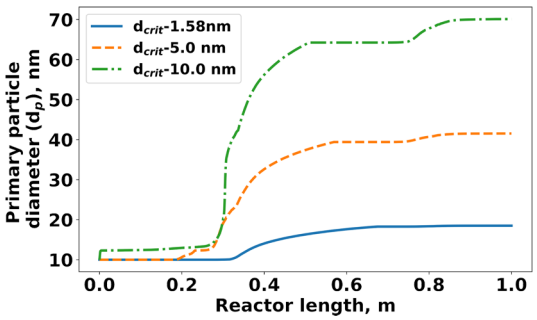

Figure 9. Effect of the critical particle diameter (d_{crit}) on the primary particle size along the reactor length. Solid line: d_{crit} = 1.58 nm. Dotted line: d_{crit} = 5.0 nm. Dashed line: d_{crit} = 10.0 nm.

Characterization Results. A typical Raman spectrum is shown in Figure 10. The rather broad bands are typical for less

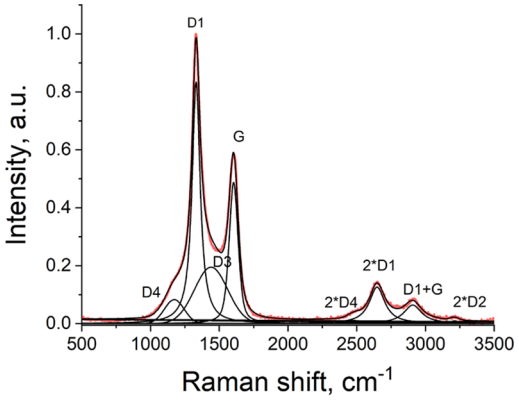

Figure 10. Deconvoluted Raman spectra and curve fitting for the soot sample at 1673 K.

ordered carbon materials due to partially overlapping, an adequate separation of these bands is difficult. In the first-order region (1100−1800 cm^{-1}), previously, a simple curve fit by two bands has often been performed, but this is insufficient for accurate structural characterization. In this study, the spectrum in the first- and second-order regions was deconvoluted to 4 peaks and a curve fitting was performed using a combination of Gaussian and Lorenzen shape bands, as shown in Figure 10.

For perfect graphite, the G band is the only one found in the first-order region, which is due to an ideal graphite lattice. For the less well-ordered carbon material studied here, additional bands appear in the first-order region around 1200 (D4), 1350 (D1), and 1500 (D3) cm^{-1}. The most intense band D1 is known to be characteristic of disordered graphite. The intensity of the D band relative to that of the G band increases with the degree of disorder. Furthermore, D4 and D3 bands are observed that occur in high-defect carbons such as carbon black and have been assigned to the presence of amorphous carbon (D3) and of hydrocarbon or aliphatic moieties bonded to graphitic basic structural units (D4).[60,61,72−74]

Raman spectra recorded for amorphous carbon and many of the soot samples exhibited broad signals (no distinct peaks) in the range from about 2300 to 3300 cm^{-1} (second-order region).[61] In this case, two pronounced peaks were observed. The band at about 2650 cm^{-1} is the strongest and can be attributed to the first overtone of the D1 band (2★D1) and the second one at 2900 cm^{-1} (D1+G) was attributed to a

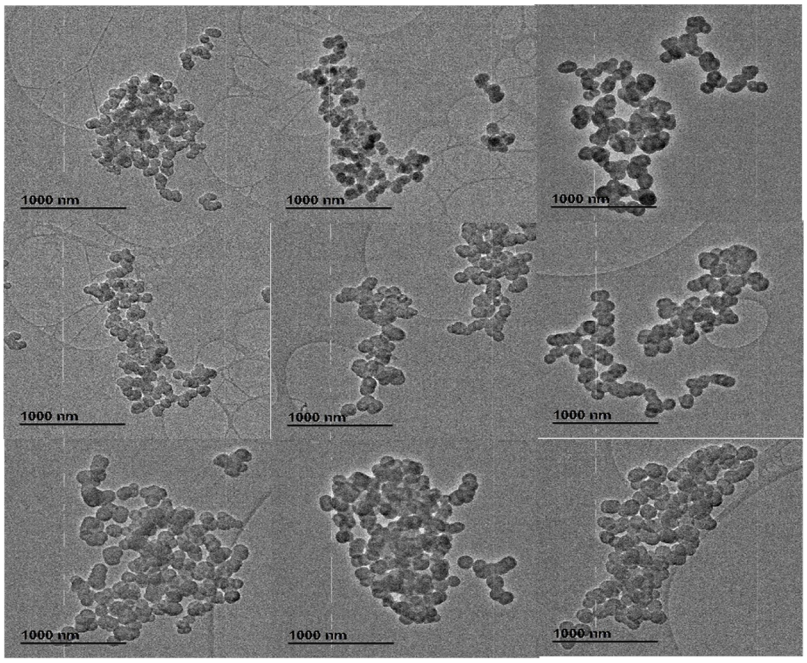

(a) Soot aggregates

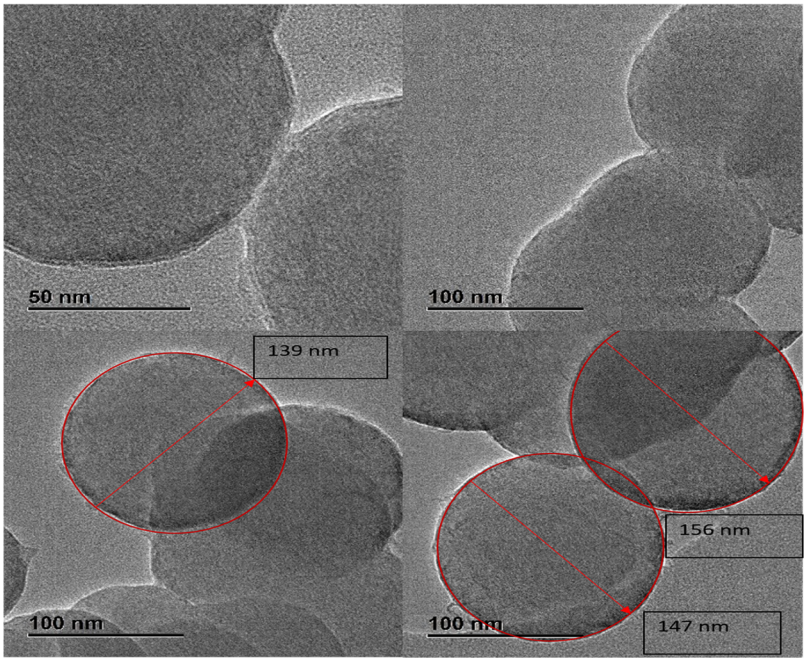

(b) Soot primary particles

Figure 11. TEM image of a soot sample obtained after 20 min of reactor operation at 1673 K.

combination of the G and D modes characteristic for disturbed graphitic structures. In an ideal graphitic structure, the D1+G peak is most pronounced and the 2*D1 bond appears as a small shoulder.

In general, the Raman spectroscopic results indicate that the soot produced in the empty reactor does not have the structure of amorphous carbon or ideal graphite. The structure is more ordered compared to amorphous carbon, as clearly indicated by the G band and the D1+G band in the spectrum. However, the discovered D bands prove some defects in the graphite structure.

From the obtained TEM analysis at 1673 K and 20 min collection time, Figure 11 shows representative images of the soot aggregates (Figure 11 (a)) and primary particles (Figure 11 (b)). Different time intervals were used to collect the soot samples: 5, 10, and 20 min. As shown in Figure S1, most of the aggregates formed after 5 min are quite small and contain few primary particles. After 10 min, larger aggregates can be seen, some growing linearly with low fractal dimension and others compactly with high fractal dimension (Figure S2). Additionally, the soot sample collected after 20 min of reactor operation shows some small aggregates, as well as larger aggregates

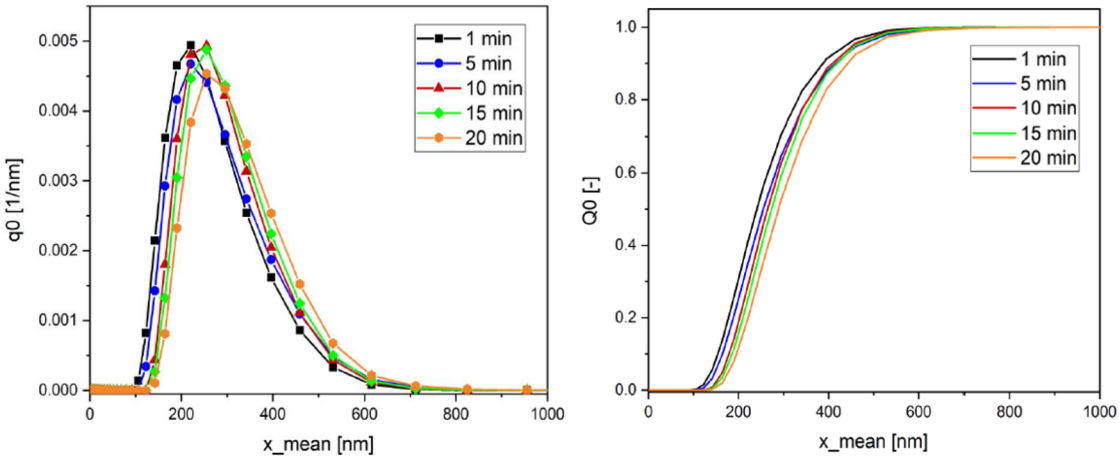

Figure 12. Soot sample number density and cumulative size distribution obtained by DLS measurements at 1673 K.

containing many primary particles (Figure 11). In each time step, soot primary particle size ranges between 140 and 160 nm, and reaction time has no significant impact on soot particle size.

A comprehensive size distribution analysis was performed with DLS on a soot sample produced at 1673 K and collected at the end of the reactor. Figure 12 depicts the number density and cumulative size distribution for soot samples obtained at different time intervals, 1, 5, 10, and 20 min, while operating the reactor at 1676 K. The soot samples were analyzed under the same conditions and setup. Based on the cumulative size distribution results, it is evident that the size of the soot aggregates increases over time. Contrary to the other three time steps, 5, 10, and 20 min, the difference between 1 and 20 min is very large. As the time step increases, the peak of the density size distribution for all samples shifts to the right toward the maximum value. The standard deviation did not change significantly, as shown in Figure 12. Furthermore, the distribution appears to be unimodal. The particles, being at high temperatures and with a longer residence time, eliminate competition between soot nucleation and coagulation processes, resulting in unimodal distribution. Table 2 provides median diameter values for soot samples produced at 1673 K; the values are the average of three measurements.

Table 2. Soot Sample Median Diameter for Volume (x_50,3) and Number (x_50,0) Size Distribution Obtained by DLS Measurements at 1673 K.

Time (min)	x_50,3 (nm)	x_50,0 (nm)
1	318.4 ± 3.9	206.6 ± 12.2
5	342.0 ± 5.8	246.8 ± 7.2
10	343.4 ± 10.0	245.4 ± 10.1
20	394.2 ± 2.3	256.5 ± 8.7

The model has demonstrated its capability in capturing the trends of soot formation, and with further expansion, it can potentially provide even more accurate predictions. A comparison of the characterization data and the numerical prediction of soot formation reveals room for improvement in the model's accuracy. Although the predicted primary particle diameters vary between 11 and 19 nm with a narrow PSD, experimental results indicate that soot consists of primary particles ranging between 140 and 160 nm with a broad particle size distribution that consists of very large particles. This discrepancy is due to the limitations and assumptions of the monodisperse model, including the lack of consideration for soot surface growth and the possibility of condensation or adsorption of PAHs on soot particles, which cause an underestimation of the primary particle diameter. Additionally, during the experiment, an almost complete consumption of C_2H_2 species was observed, which is thought to contribute to soot surface growth and carbon deposition. The present experimental study and findings by Lott et al.[71] indicate that C_2H_2 species are involved in both the formation of graphitic sheet-like carbon (via a deposition mechanism) and soot formation (via a surface growth mechanism). Moreover, the diameter of the primary particles was strongly influenced by the sintering rate. It was observed that the highest value was 19 nm at 1673 K, while the smallest value was 11 nm at 1473 K. Although the present simulation does not take soot surface growth due to C_2H_2 into consideration, the sintering phenomenon alone results in a considerable increase in primary particle diameter. Hence, to simulate soot formation in a flow reactor under pyrolytic conditions, it is imperative to take sintering into account. Notably, despite its limitations, the model is capable of capturing the general trend in the relationship between temperature and soot formation. On the other hand, our current results suggest that more advanced soot models that will be developed in the future need to include factors like sintering, surface growth, and deposition, herewith preferably relying on profound 2D and 3D characterization studies that ultimately allow us to congruently model the formation of soot particles.[75]

CONCLUSIONS

A one-dimension plug-flow reactor model was coupled with a monodisperse model (three equation systems) involving simultaneous chemical reaction, coagulation, and sintering. Soot formation during methane pyrolysis is simulated using detailed chemical kinetics, and the profiles for the mole fractions of the major species H_2 and CH_4 and minor species C_2H_2, C_2H_4, C_2H_6, C_6H_6, $C_{10}H_8$, $C_{14}H_{10}$, and $C_{16}H_{10}$ are determined along the length of the reactor. Experimental studies provide information on the mole fraction of major and minor species. Although the simulation showed good agreement with the experimental data for end-of-pipe mole fractions of CH_4 and H_2, a discrepancy was found for intermediate species (minors). Additionally, the simulation showed that the

highest methane conversion was achieved at the hot zone temperature of 1673 K, compared to results at 1473 and 1873 K, which was primarily attributed to thermodynamic limitations.

In the absence of oxygen, the highest nucleation rate during methane pyrolysis occurs at 1673 K. Analysis of the particle number concentrations indicates an initial increase due to nucleation, followed by a decrease due to coagulation. At 1673 K, the model predicted a maximum primary particle diameter of 19 nm over a PSD range of 10−100 nm. A TEM image and Raman spectrum of the collected soot samples revealed that it is composed of amorphous agglomerated primary particles around 150 nm in diameter. There are crystalline and amorphous domains in soot samples, with the turbostratically stacked graphene layers usually forming crystalline domains. Additionally, downstream of the hot zone, the number of primary particles per aggregate and soot mass increased, mostly because of a decrease in nucleation and an increase in coagulation. The comparison between numerical and experimental studies indicates that the gas-phase chemical kinetics model, although it predicted all the trends of the gaseous conversion in the reactor, has been insufficient for the pyrolysis of methane. Even though the pyrene dimer was chosen to be responsible for soot nucleation, experiments and numerical simulations show that other PAHs also form in substantial amounts. Consequently, other PAHs need to be included in the chemical source term for monodisperse models to enhance the term. Alternatively, it would be helpful to integrate additional factors into the model that may affect the vdW enhancement factor and the collision efficiency of the particles, such as particle size, shape, and surface chemistry. Notably, this approach would be a step toward more realistic models of soot formation that consider the full complexity of chemical reactions leading to the formation of particles of soot. In addition, the experimental study showed that nearly all C_2H_2 species are consumed, which contributes to soot surface growth and graphitic sheet-like carbon deposits. This provides a basis for future studies to investigate the role of C_2H_2 species in more detail. Although it has limitations in its complexity, the monodisperse model is computationally less demanding and provides insight into the underlying physical and chemical processes that govern the system's behavior.

Further work will include systematic advanced experiments to improve the kinetics in addition to the above processes. To gain a better understanding of soot particles' 3-D structure, a tomography study will be conducted. Despite this, the present model provides a solid basis for studying nanoparticles and soot growth in complex flows based on detailed chemical kinetics.

AUTHOR INFORMATION

Corresponding Author

Olaf Deutschmann − *Institute for Chemical Technology and Polymer Chemistry, Karlsruhe Institute of Technology (KIT), 76131 Karlsruhe, Germany; Institute of Catalysis Research and Technology, Karlsruhe Institute of Technology (KIT), 76344 Eggenstein-Leopoldshafen, Germany;* orcid.org/0000-0001-9211-7529; Phone: +49 721 608 43064; Email: deutschmann@kit.edu

Authors

Akash Bhimrao Shirsath − *Institute for Chemical Technology and Polymer Chemistry, Karlsruhe Institute of Technology (KIT), 76131 Karlsruhe, Germany*

Manas Mokashi − *Institute for Chemical Technology and Polymer Chemistry, Karlsruhe Institute of Technology (KIT), 76131 Karlsruhe, Germany*

Patrick Lott − *Institute for Chemical Technology and Polymer Chemistry, Karlsruhe Institute of Technology (KIT), 76131 Karlsruhe, Germany;* orcid.org/0000-0001-8683-2155

Heinz Müller − *Institute for Chemical Technology and Polymer Chemistry, Karlsruhe Institute of Technology (KIT), 76131 Karlsruhe, Germany*

Reihaneh Pashminehazar − *Institute for Chemical Technology and Polymer Chemistry, Karlsruhe Institute of Technology (KIT), 76131 Karlsruhe, Germany*

Thomas Sheppard − *Institute for Chemical Technology and Polymer Chemistry, Karlsruhe Institute of Technology (KIT), 76131 Karlsruhe, Germany;* orcid.org/0000-0002-8891-985X

Steffen Tischer − *Institute of Catalysis Research and Technology, Karlsruhe Institute of Technology (KIT), 76344 Eggenstein-Leopoldshafen, Germany;* orcid.org/0000-0002-9272-5556

Lubow Maier − *Institute of Catalysis Research and Technology, Karlsruhe Institute of Technology (KIT), 76344 Eggenstein-Leopoldshafen, Germany*

Jan-Dierk Grunwaldt − *Institute for Chemical Technology and Polymer Chemistry, Karlsruhe Institute of Technology (KIT), 76131 Karlsruhe, Germany; Institute of Catalysis Research and Technology, Karlsruhe Institute of Technology (KIT), 76344 Eggenstein-Leopoldshafen, Germany;* orcid.org/0000-0003-3606-0956

Notes

The authors declare no competing financial interest.

ACKNOWLEDGMENTS

The authors gratefully acknowledge funding by the Federal Ministry of Education and Research (BMBF) of Germany, project Me2H2, grant number 03SF0571A-G. The Steinbeis GmbH für Technologietransfer (STZ 240 Reaktive Strömung) is gratefully acknowledged for a cost-free academic license of DETCHEM. Institute of Nanotechnology, Karlsruhe Nano Micro Facility, Karlsruhe Institute of Technology is gratefully acknowledged for TEM analysis. The authors gratefully acknowledge David Gaus, Institute of Thermal Process Engineering, Karlsruhe Institute of Technology, for DLS analysis. The authors also acknowledge Karlsruhe Institute of Technology and DFG for financing the Raman spectrometer system (INST 121384/731).

REFERENCES

(1) Giehr, A.; Maier, L.; Angeli, S.; Schunk, S. A.; Deutschmann, O. Dry and Steam Reforming of CH_4 on Co-Hexaaluminate: On the Formation of Metallic Co and Its Influence on Catalyst Activity. *Ind. Eng. Chem. Res.* **2020**, *59*, 18790−18797.

(2) Wittich, K.; Krämer, M.; Bottke, N.; Schunk, S. A. Catalytic Dry Reforming of Methane: Insights from Model Systems. *ChemCatChem* **2020**, *12*, 2130−2147.
(3) Machhammer, O.; Bode, A.; Hormuth, W. Financial and Ecological Evaluation of Hydrogen Production Processes on Large Scale. *Chem. Eng. Technol.* **2016**, *39*, 1185−1193.
(4) Sánchez-Bastardo, N.; Schlögl, R.; Ruland, H. Methane Pyrolysis for CO_2-Free H_2 Production: A Green Process to Overcome Renewable Energies Unsteadiness. *Chem.-Ing.-Tech.* **2020**, *92*, 1596−1609.
(5) Ehrhardt, K.; Scheiff, F.; Flick, D.; Lott, P.; Mokashi, M.; Heitlinger, H.; Pashminehazar, R.; Shirsath, A.; Müller, H.; Lichtenberg, S. et al. Pyrolysis of methane: interplay between industrial design considerations and detailed chemistry evaluation. *13th European Congress of Chemical Engineering*; ECCE-ECAB, 2021.
(6) Lott, P.; Deutschmann, O. Heterogeneous chemical reactions-A cornerstone in emission reduction of local pollutants and greenhouse gases. *Proceedings of the Combustion Institute* **2022**, DOI: 10.1016/j.proci.2022.06.001.
(7) Becker, A.; Hüttinger, K. Chemistry and kinetics of chemical vapor deposition of pyrocarbon - IV pyrocarbon deposition from methane in the low temperature regime. *Carbon* **1998**, *36*, 213−224.
(8) Li, A.; Schoch, G.; Lichtenberg, S.; Zhang, D.; Deutschmann, O. A novel CVD/CVI reactor with an in-situ sampling apparatus connected to an online GC/MS. *Surf. Coat. Technol.* **2007**, *201*, 8939−8943.
(9) Bockhorn, H. *Soot formation in combustion: mechanisms and models*; Springer Science & Business Media, 2013; Vol. *59*.
(10) Gebert, J. M.; Reznik, B.; Piat, R.; Viering, B.; Weidenmann, K.; Wanner, A.; Deutschmann, O. Elastic constants of high-texture pyrolytic carbon measured by ultrasound phase spectroscopy. *Carbon* **2010**, *48*, 3647−3650.
(11) Norinaga, K.; Deutschmann, O.; Hüttinger, K. J. Analysis of gas phase compounds in chemical vapor deposition of carbon from light hydrocarbons. *Carbon* **2006**, *44*, 1790−1800.
(12) Reznik, B.; Norinaga, K.; Gerthsen, D.; Deutschmann, O. The effect of cooling rate on hydrogen release from a pyrolytic carbon coating and its resulting morphology. *Carbon* **2006**, *44*, 1330−1334.
(13) Appel, J.; Bockhorn, H.; Frenklach, M. Kinetic modeling of soot formation with detailed chemistry and physics: laminar premixed flames of C_2 hydrocarbons. *Combust. Flame* **2000**, *121*, 122−136.
(14) Frenklach, M.; Wang, H. Detailed modeling of soot particle nucleation and growth. *Symposium (International) on Combustion* **1991**, *23*, 1559−1566.
(15) Bockhorn, H.; Geitlinger, H.; Jungfleisch, B.; Lehre, T.; Schön, A.; Streibel, T.; Suntz, R. Progress in characterization of soot formation by optical methods. *Phys. Chem. Chem. Phys.* **2002**, *4*, 3780−3793.
(16) Mauss, F.; Schäfer, T.; Bockhorn, H. Inception and growth of soot particles in dependence on the surrounding gas phase. *Combust. Flame* **1994**, *99*, 697−705.
(17) Tesner, P. A.; Shurupov, S. V. Some Physico-Chemical Parameters of Soot Formation During Pyrolysis of Hydrocarbons. *Combust. Sci. Technol.* **1995**, *105*, 147−161.
(18) Tesner, P. A.; Shurupov, S. V. Soot formation during pyrolysis of naphthalene, anthracene and pyrene. *Combust. Sci. Technol.* **1997**, *126*, 139−151.
(19) Yapp, E. K.; Chen, D.; Akroyd, J.; Mosbach, S.; Kraft, M.; Camacho, J.; Wang, H. Numerical simulation and parametric sensitivity study of particle size distributions in a burner-stabilised stagnation flame. *Combust. Flame* **2015**, *162*, 2569−2581.
(20) Frenklach, M. Reaction mechanism of soot formation in flames. *Phys. Chem. Chem. Phys.* **2002**, *4*, 2028−2037.
(21) Tsantilis, S.; Pratsinis, S. E. Soft- and hard-agglomerate aerosols made at high temperatures. *Langmuir* **2004**, *20*, 5933−5939.
(22) Spicer, P. T.; Chaoul, O.; Tsantilis, S.; Pratsinis, S. E. Titania formation by $TiCl_4$ gas phase oxidation, surface growth and coagulation. *Journal of Aerosol Science* **2002**, *33*, 17−34.
(23) Kelesidis, G. A.; Kholghy, M. R. A monodisperse population balance model for nanoparticle agglomeration in the transition regime. *Materials* **2021**, *14*, 3882.
(24) Kruis, F. E.; Kusters, K. A.; Pratsinis, S. E.; Scarlett, B. A Simple Model for the Evolution of the Characteristics of Aggregate Particles Undergoing Coagulation and Sintering. *Aerosol Sci. Technol.* **1993**, *19*, 514−526.
(25) Frenklach, M.; Wang, H. *Soot Formation in Combustion: Mechanisms and Models*; Springer Berlin Heidelberg: Berlin, Heidelberg, 1994; pp 165−192.
(26) Frenklach, M.; Harris, S. J. Aerosol dynamics modeling using the method of moments. *Journal of Colloid And Interface Science* **1987**, *118*, 252−261.
(27) Zhao, B.; Yang, Z.; Johnston, M. V.; Wang, H.; Wexler, A. S.; Balthasar, M.; Kraft, M. Measurement and numerical simulation of soot particle size distribution functions in a laminar premixed ethylene-oxygen-argon flame. *Combust. Flame* **2003**, *133*, 173−188.
(28) Pope, C. J.; Howard, J. B. Simultaneous particle and molecule modeling (spamm): An approach for combining sectional aerosol equations and elementary gas-phase reactions. *Aerosol Sci. Technol.* **1997**, *27*, 73−94.
(29) Aubagnac-Karkar, D.; El Bakali, A.; Desgroux, P. Soot particles inception and PAH condensation modelling applied in a soot model utilizing a sectional method. *Combust. Flame* **2018**, *189*, 190−206.
(30) Wen, J. Z.; Thomson, M. J.; Park, S. H.; Rogak, S. N.; Lightstone, M. F. Study of soot growth in a plug flow reactor using a moving sectional model. *Proceedings of the Combustion Institute* **2005**, *30*, 1477−1484.
(31) Balthasar, M.; Kraft, M. A stochastic approach to calculate the particle size distribution function of soot particles in laminar premixed flames. *Combust. Flame* **2003**, *133*, 289−298.
(32) Appel, J.; Bockhorn, H.; Wulkow, M. A detailed numerical study of the evolution of soot particle size distributions in laminar premixed flames. *Chemosphere* **2001**, *42*, 635−645.
(33) Miller, J. H. Aromatic excimers: Evidence for polynuclear aromatic hydrocarbon condensation in flames. *Proceedings of the Combustion Institute* **2005**, *30*, 1381−1388.
(34) Wartel, M.; Pauwels, J. F.; Desgroux, P.; Mercier, X. Pyrene measurements in sooting low pressure methane flames by jet-cooled laser-induced fluorescence. *Journal of Physical Chemistry A* **2011**, *115*, 14153−14162.
(35) Le, K. C.; Lefumeux, C.; Pino, T. Watching soot inception via online Raman spectroscopy. *Combust. Flame* **2022**, *236*, 111817.
(36) Wang, Y.; Raj, A.; Chung, S. H. Soot modeling of counterflow diffusion flames of ethylene-based binary mixture fuels. *Combust. Flame* **2015**, *162*, 586−596.
(37) Wang, Y.; Raj, A.; Chung, S. H. A PAH growth mechanism and synergistic effect on PAH formation in counterflow diffusion flames. *Combust. Flame* **2013**, *160*, 1667−1676.
(38) Sabbah, H.; Biennier, L.; Klippenstein, S. J.; Sims, I. R.; Rowe, B. R. Exploring the role of PAHs in the formation of soot: Pyrene dimerization. *Journal of Physical Chemistry Letters* **2010**, *1*, 2962−2967.
(39) Frenklach, M.; Mebel, A. M. On the mechanism of soot nucleation. *Phys. Chem. Chem. Phys.* **2020**, *22*, 5314−5331.
(40) Schuetz, C. A.; Frenklach, M. Nucleation of soot: Molecular dynamics simulations of pyrene dimerization. *Proceedings of the Combustion Institute* **2002**, *29*, 2307−2314.
(41) Desgroux, P.; Faccinetto, A.; Mercier, X.; Mouton, T.; Aubagnac Karkar, D.; El Bakali, A. Comparative study of the soot formation process in a "nucleation" and a "sooting" low pressure premixed methane flame. *Combust. Flame* **2017**, *184*, 153−166.
(42) Faccinetto, A.; Irimiea, C.; Minutolo, P.; Commodo, M.; D'Anna, A.; Nuns, N.; Carpentier, Y.; Pirim, C.; Desgroux, P.; Focsa, C.; Mercier, X. Evidence on the formation of dimers of polycyclic aromatic hydrocarbons in a laminar diffusion flame. *Communications Chemistry* **2020**, *3*, 112.
(43) Hou, D.; Lindberg, C. S.; Manuputty, M. Y.; You, X.; Kraft, M. Modelling soot formation in a benchmark ethylene stagnation flame

with a new detailed population balance model. *Combust. Flame* **2019**, *203*, 56−71.
(44) Shekar, S.; Smith, A. J.; Menz, W. J.; Sander, M.; Kraft, M. A multidimensional population balance model to describe the aerosol synthesis of silica nanoparticles. *Journal of Aerosol Science* **2012**, *44*, 83−98.
(45) Tsantilis, S.; Pratsinis, S. E.; Briesen, H. Sintering Time for Silica Particle Growth. *Aerosol Sci. Technol.* **2001**, *34*, 237−246.
(46) Zachariah, M. R.; Carrier, M. J. Molecular dynamics computation of gas-phase nanoparticle sintering: A comparison with phenomenological models. *Journal of Aerosol Science* **1999**, *30*, 1139−1151.
(47) Chen, D.; Zainuddin, Z.; Yapp, E.; Akroyd, J.; Mosbach, S.; Kraft, M. A fully coupled simulation of PAH and soot growth with a population balance model. *Proceedings of the Combustion Institute* **2013**, *34*, 1827−1835.
(48) Sander, M.; West, R. H.; Celnik, M. S.; Kraft, M. A detailed model for the sintering of polydispersed nanoparticle agglomerates. *Aerosol Sci. Technol.* **2009**, *43*, 978−989.
(49) Haynes, B. S.; Wagner, H. G. Soot formation. *Prog. Energy Combust. Sci.* **1981**, *7*, 229−273.
(50) Wersborg, B. L.; Howard, J. B.; Williams, G. C. Physical mechanisms in carbon formation in flames. *Symposium (International) on Combustion* **1973**, *14*, 929−940.
(51) Park, S. H.; Rogak, S. N.; Bushe, W. K.; Wen, J. Z.; Thomson, M. J. An aerosol model to predict size and structure of soot particles. *Combustion Theory and Modelling* **2005**, *9*, 499−513.
(52) Morgan, N. M.; Patterson, R. I.; Kraft, M. Modes of neck growth in nanoparticle aggregates. *Combust. Flame* **2008**, *152*, 272−275.
(53) Ono, K.; Dewa, K.; Matsukawa, Y.; Saito, Y.; Matsushita, Y.; Aoki, H.; Era, K.; Aoki, T.; Yamaguchi, T. Experimental evidence for the sintering of primary soot particles. *Journal of Aerosol Science* **2017**, *105*, 1−9.
(54) Chen, D.; Totton, T. S.; Akroyd, J.; Mosbach, S.; Kraft, M. Phase change of polycyclic aromatic hydrocarbon clusters by mass addition. *Carbon* **2014**, *77*, 25−35.
(55) Leung, K. M.; Lindstedt, R. P.; Jones, W. P. A simplified reaction mechanism for soot formation in nonpremixed flames. *Combust. Flame* **1991**, *87*, 289−305.
(56) Grass, R. N.; Tsantilis, S.; Pratsinis, S. E. Design of high-temperature, gas-phase synthesis of hard or soft TiO_2 agglomerates. *AIChE J.* **2006**, *52*, 1318−1325.
(57) Kholghy, M. R.; Kelesidis, G. A. Surface growth, coagulation and oxidation of soot by a monodisperse population balance model. *Combust. Flame* **2021**, *227*, 456−463.
(58) Deutschmann, O.; Tischer, S.; Kleditzsch, S.; Janardhanan, V.; Correa, C.; Chatterjee, D.; Mladenov, N.; Minh, H. D.; Karadeniz, H.; Hettel, M.; Menon, V.; Banerjee, A.; Gossler, H.; Shirsath, A.; Daymo, E. *DETCHEM*; 2022; https://www.detchem.com.
(59) Angeli, S. D.; Gossler, S.; Lichtenberg, S.; Kass, G.; Agrawal, A. K.; Valerius, M.; Kinzel, K. P.; Deutschmann, O. Reduction of CO_2 Emission from Off-Gases of Steel Industry by Dry Reforming of Methane. *Angewandte Chemie - International Edition* **2021**, *60*, 11852−11857.
(60) Bokobza, L.; Bruneel, J.-L.; Couzi, M. Raman Spectra of Carbon-Based Materials (from Graphite to Carbon Black) and of Some Silicone Composites. *C* **2015**, *1*, 77−94.
(61) Sadezky, A.; Muckenhuber, H.; Grothe, H.; Niessner, R.; Pöschl, U. Raman microspectroscopy of soot and related carbonaceous materials: Spectral analysis and structural information. *Carbon* **2005**, *43*, 1731−1742.
(62) Böttcher, A.; Hennrich, F.; Rösner, H.; Malik, S.; Kappes, M. M.; Lichtenberg, S.; Schoch, G.; Deutschmann, O. Growth of novel carbon phases by methane infiltration of free-standing single-walled carbon nanotube films. *Carbon* **2007**, *45*, 1085−1096.
(63) Kholghy, M. R.; Kelesidis, G. A.; Pratsinis, S. E. Reactive polycyclic aromatic hydrocarbon dimerization drives soot nucleation. *Phys. Chem. Chem. Phys.* **2018**, *20*, 10926−10938.
(64) Deutschmann, O. Modeling of the Interactions Between Catalytic Surfaces and Gas-Phase. *Catal. Lett.* **2015**, *145*, 272−289.
(65) Herrera Delgado, K.; Maier, L.; Tischer, S.; Zellner, A.; Stotz, H.; Deutschmann, O. Surface reaction kinetics of steam- and CO_2-reforming as well as oxidation of methane over nickel-based catalysts. *Catalysts* **2015**, *5*, 871−904.
(66) Deuflhard, P.; Hairer, E.; Zugck, J. One-step and extrapolation methods for differential-algebraic systems. *Numerische Mathematik* **1987**, *51*, 501−516.
(67) Seinfeld, J. H. ESTBooks. *Environ. Sci. Technol.* **1986**, *20*, 863−863.
(68) Wang, Y.; Liu, F.; He, C.; Bi, L.; Cheng, T.; Wang, Z.; Zhang, H.; Zhang, X.; Shi, Z.; Li, W. Fractal Dimensions and Mixing Structures of Soot Particles during Atmospheric Processing. *Environmental Science and Technology Letters* **2017**, *4*, 487−493.
(69) Kelesidis, G. A.; Goudeli, E.; Pratsinis, S. E. Morphology and mobility diameter of carbonaceous aerosols during agglomeration and surface growth. *Carbon* **2017**, *121*, 527−535.
(70) Frenklach, M. On surface growth mechanism of soot particles. *Symposium (International) on Combustion* **1996**, *26*, 2285−2293.
(71) Lott, P.; Mokashi, M. B.; Müller, H.; Heitlinger, D. J.; Lichtenberg, S.; Shirsath, A. B.; Janzer, C.; Tischer, S.; Maier, L.; Deutschmann, O. Hydrogen Production and Carbon Capture by Gas-Phase Methane Pyrolysis: A Feasibility Study. *ChemSusChem* **2022**, e202201720.
(72) Vázquez-Santos, M. B.; Geissler, E.; László, K.; Rouzaud, J. N.; Martínez-Alonso, A.; Tascón, J. M. Comparative XRD, Raman, and TEM study on graphitization of PBO-derived carbon fibers. *Journal of Physical Chemistry C* **2012**, *116*, 257−268.
(73) Zhang, W.; Reznik, B.; Deutschmann, O. Raman microprobe spectrometry of carbon/carbon composites with differently-textured pyrolytic carbon matrices. *ZAMM Zeitschrift fur Angewandte Mathematik und Mechanik* **2013**, *93*, 329−337.
(74) Mutz, B.; Sprenger, P.; Wang, W.; Wang, D.; Kleist, W.; Grunwaldt, J.-D. Operando Raman spectroscopy on CO_2 methanation over alumina-supported Ni, Ni_3Fe and NiRh0.1 catalysts: Role of carbon formation as possible deactivation pathway. *Applied Catalysis A: General* **2018**, *556*, 160−171.
(75) Grunwaldt, J.-D.; Wagner, J. B.; Dunin-Borkowski, R. E. Imaging Catalysts at Work: A Hierarchical Approach from the Macro- to the Meso- and Nano-scale. *ChemCatChem* **2013**, *5*, 62−80.